Compressibility Effects in Slender Rocket Motors

Michel Akiki[*] and Joseph Majdalani[†]
University of Tennessee Space Institute, Tullahoma, TN 37388

In this article, a semi-analytical formulation is provided for the rotational, steady, inviscid, compressible motion of a solid rocket motor that is modeled as a slender porous chamber. The analysis overcomes some of the deficiencies encountered in previous work on the subject. The method that we employ consists of reducing the problem's mass, momentum, energy, ideal gas, and isentropic relations into a single integral equation that can be solved numerically. Furthermore, Saint-Robert's power law representation is used to link the pressure to the sidewall mass injection rate. At the outset, results are presented for the axisymmetric porous cylinder and compared to two closed-form analytical solutions developed under one-dimensional and two-dimensional, isentropic flow conditions. The comparison is carried out assuming either uniformly distributed mass flux or constant radial injection speed along the porous wall. Our amended formulation is shown to agree with the one-dimensional solution obtained for the case of uniform wall mass flux and with the asymptotic approximation obtained by Majdalani for the constant wall injection speed (Majdalani, J., On Steady Rotational High Speed Flows: The Compressible Taylor-Culick Profile, Proceedings of the Royal Society of London, Series A: Mathematical, Physical and Engineering Sciences, Vol. 463, No. 2077, 2007, pp. 131-162). While all solutions agree on the critical distance to reach sonic conditions, differences among them occur near choking and these could be partly attributed to the level of approximation entailed in the integral approximation.

Nomenclature

a	=	chamber radius
c_p	=	constant pressure specific heat
L_0	=	length of chamber
L_s	=	sonic length (critical distance)
M	=	Mach number
m	=	injection mass flux
P	=	nondimensional pressure
p	=	dimensional pressure
r	=	coordinate normal to the propellant surface
T	=	temperature
U_w	=	wall injection velocity
u	=	axial velocity
v	=	radial velocity
X	=	nondimensional axial coordinate
x	=	dimensional axial coordinate

Greek

ψ	=	stream function
χ	=	axial coordinate referenced to the sonic length, x/L_s
γ	=	ratio of specific heats
ρ	=	density

[*]Graduate Research Assistant, Mechanical, Aerospace and Biomedical Engineering Department. Member AIAA.
[†]H. H. Arnold Chair of Excellence in Advanced Propulsion, Mechanical, Aerospace and Biomedical Engineering Department. Senior Member AIAA. Fellow ASME.

ξ =   distance from the headwall to the tip of the streamline at the sidewall

Subscripts
c   =   chocking or centerline conditions
w   =   wall conditions

I. Introduction

SOLID rocket motors are often idealized as porous channels and ducts in which the effects of compressibility can be either retained or dismissed, depending on the gas injection speed and chamber length. While the incompressible motion is relatively well understood,[1-2] recent advances have enabled us to account for the presence of arbitrary headwall injection,[3-4] wall regression,[5-6] grain taper,[7-8] and variable cross-section.[9] Furthermore, flow approximations exhibiting smoother or steeper profiles than the cold flow equilibrium state have been studied in connection with their energy content.[10-11] As for compressible flow effects, these have been first investigated by Dunlap, Willoughby and Hermsen,[12] and Traineau, Hervat and Kuentzmann[13] in the context of two-dimensional porous tubes and channels with sidewall injection. Using either Nitrogen or air as the working substance, these investigators have reported rich characteristics of the spatially developing motion including appreciable steepening beyond the Taylor-Culick baseline.[1-2] In the downstream sections of the domain, compressibility intensified to the extent of producing noticeably flattened mean flow profiles. These observations were further supported by numerical simulations attributed to Beddini,[14] Baum, Levine and Lovine,[15] Liou and Lien,[16] and Apte and Yang.[17-18] They were also studied by Gany and Aharon[19] and King[20] in the context of nozzleless rocket motors. While the former group explored the merits of a one-dimensional theoretical model, the latter employed a pseudo two-dimensional numerical approach. Given the relevance of an accurate mean flow description to the study of hydrodynamic instability in simulated rocket motors, the problem was revisited by Venugopal, Najjar and Moser[21] and, in complementary work, by Wasistho, Balachandar, and Moser.[22] As a windfall, the compressible solutions engendered in these studies proved to be valuable resources for verifying numerical results obtained from full-scale Navier-Stokes solvers.[23-24] This was partly caused by the obstacles placed against the acquisition of specific experimental data and, partly, because of the intrusion-resistant environment in rocket chambers.

Among the analytical techniques that have been applied to this problem, the first may be the Prandtl-Glauert expansion.[25] In fact, a variant of this technique was used by Traineau, Hervat and Kuentzmann[13] who introduced, in a precursor to the present study, an inviscid, rotational, and compressible integral equation that can be solved in a planar, two dimensional setting. In addition to their elegant analytical and numerical work, they produced a collection of experimental data based on cold flow measurements that utilized air as the sidewall injectant. In their analytical effort, these investigators have utilized judicious scaling arguments to justify the dismissal of the radial momentum equation, thereby reducing the remaining momentum, mass, energy, ideal gas, and isentropic state relations to a single integral expression that can be numerically solved for the pressure distribution. Furthermore, their pressure and wall mass flux were related through the Saint-Robert power law, and their Abel integral equation could be shown to be soluble analytically in the case for which $2(2-\gamma)/(\gamma-1)$ took on an integer value.

In mirroring the aforementioned work, Balakrishnan, Liñan and Williams[26] sought to reconstruct an inviscid, rotational, and compressible integral formulation for the porous channel problem. However, in their attempt at replicating the effort of Traineau and co-workers,[13] these researchers have inadvertently produced a planar solution that contained multiple blunders. These were partly rectified in a follow-up sequel in which both axisymmetric and planar settings were discussed.[27]

The second analytical approach used in this context consists of a variant of the Rayleigh-Janzen expansion. This asymptotic technique is based on small parameter perturbations in the square of the wall injection Mach number. The Rayleigh-Janzen expansion was first applied by Majdalani[28] in the treatment of the axisymmetric porous cylinder and by Maicke and Majdalani[29] in the planar flow analog. The axisymmetric analysis led to two closed-form solutions, one exact, satisfying all first principles, and one approximate, essentially equivalent alternative. The planar effort gave rise to a single compact expression satisfying all physical requirements. In consequence, both streamwise and wall-normal velocity profiles could be readily calculated in addition to the critical length needed to achieve sonic conditions. Moreover, the effort led to the identification of the sonic distance as the appropriate lengthscale which, when inserted into the solution, would promote a self-similar, parameter-independent behavior for all wall Mach numbers. It also disclosed a simple criterion that could help to determine the relative effects of compressibility and the centerline amplification during flow development. By circumventing the need to compute

the mean flow over the fluid domain, the resulting expressions opened up new avenues for carrying out parametric trade analyses.

With the advent of a closed-form analytical solution for the internal burning porous cylinder in two dimensions, it is the purpose of this study to reconstruct the integral formulation developed initially by Traineau, Hervat and Kuentzmann[13] and later reproduced by Balakrishnan, Liñan and Williams.[27] Our objective is to obtain a clear and verifiable pseudo-two-dimensional approximation that could be compared to the one- and two-dimensional closed-form representations.

II. Mathematical Model

A. Geometry

We consider the steady, inviscid flow of an ideal gas in a cylinder of length L_0 and radius a. A schematic diagram of the problem considered is presented in Fig. 1. The origin of the coordinate system is located at the center of the headwall. Due to axisymmetry, half of the chamber will be investigated. Note that ψ represents a streamline and ξ denotes the axial distance from the headwall to the point where a streamline is born at the sidewall i.e., the tip of a streamline.

B. Formulation

A solid rocket motor is often idealized as a slender, elongated chamber with sidewall injection.[26-27] Under the assumption of low chamber aspect ratio, $a/L_0 \ll 1$, the system's conservation equations may be conveniently reduced to the following set:

$$\frac{\partial(\rho u r)}{\partial x} + \frac{\partial(\rho v r)}{\partial r} = 0 \ \ \text{(compressible continuity)} \tag{1}$$

$$\rho u \frac{\partial u}{\partial x} + \rho v \frac{\partial u}{\partial r} = -\frac{\partial p}{\partial x} \ \ \text{(axial momentum)} \tag{2}$$

$$\frac{\partial p}{\partial r} = 0 \ \ \text{(radial momentum)} \tag{3}$$

and

$$\rho u \frac{\partial}{\partial x}\left(c_p T + \frac{u^2}{2}\right) + \rho v \frac{\partial}{\partial r}\left(c_p T + \frac{u^2}{2}\right) = 0 \ \ \text{(energy)} \tag{4}$$

Note that pressure variations have been discounted in the radial direction due to the chamber's low aspect ratio. Furthermore, the gas may be taken to be ideal and calorically perfect, thus resulting in a constant c_p. At the outset, one may write

$$p = \frac{\gamma - 1}{\gamma} c_p \rho T \ \ \text{(ideal gas)} \tag{5}$$

At this point, Eq. (4) may be expanded and rearranged into
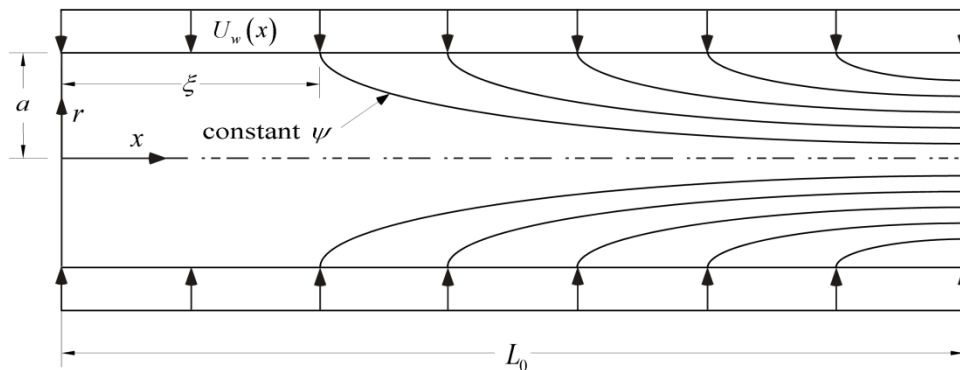
Figure 1.   Schematic diagram of a slender porous chamber.

American Institute of Aeronautics and Astronautics

$$\rho u c_p \frac{\partial T}{\partial x} + \rho v c_p \frac{\partial T}{\partial r} + u \left(\rho u \frac{\partial u}{\partial x} + \rho v \frac{\partial u}{\partial r} \right) = 0 \tag{6}$$

Both Eqs. (2) and (5) may then be substituted into Eq. (6) to produce

$$\rho u \left(\frac{\partial T}{\partial x} - \frac{\gamma - 1}{\gamma} \frac{T}{p} \frac{\partial p}{\partial x} \right) + \rho v \frac{\partial T}{\partial r} = 0 \tag{7}$$

Finally, inserting the isentropic relation, $\phi = T / p^{[(\gamma-1)/\gamma]}$, into Eq. (7), one obtains

$$\rho u \frac{\partial \phi}{\partial x} + \rho v \frac{\partial \phi}{\partial r} = 0, \qquad \rho \boldsymbol{u} \cdot \nabla \phi = 0, \quad \text{or} \quad \rho \frac{\mathrm{D}\phi}{\mathrm{D}t} = 0 \tag{8}$$

Since the material derivative vanishes in Eq. (8), it is clear that ϕ remains constant along a streamline.

C. Boundary Conditions

The physical requirements at the sidewall, headwall, and centerline are enumerated below:

$$\begin{cases} u(x,a) = 0 & \text{(no slip at sidewall)} \\ u(0,r) = 0 & \text{(no headwall injection)} \\ v(x,a) = -U_w(x) & \text{(radial sidewall injection)} \\ v(x,0) = 0 & \text{(no cross-flow at the centerline)} \\ T(x,a) = T_w(x) & \text{(sidewall temperature)} \\ p(0) = p_0 & \text{(headwall pressure)} \end{cases} \tag{9}$$

Moreover, the pressure $p = p(x)$ is permitted to evolve only with respect to x as a result of the slender motor assumption, $a/L_0 \ll 1$, and in view of Eq. (3). Meanwhile, the temperature and the velocity profiles are allowed to retain their two-dimensional aspects and can be determined as functions of both x and r.

D. Stream Function Transformation

For axisymmetric motions, the stream function may be written as

$$\frac{\partial \psi}{\partial r} = \rho u r \tag{10}$$

$$\frac{\partial \psi}{\partial x} = -\rho v r \tag{11}$$

Given that the stagnation enthalpy, $\left(c_p T + u^2 / 2 \right)$, remains invariant along a streamline, one can put

$$T(x,\psi) + u^2(x,\psi)/(2c_p) = T_w(\psi) \tag{12}$$

where $T_w(\psi)$ is the total, stagnation temperature along a streamline. Likewise for ϕ, the isentropic pressure-temperature relation may be expressed as

$$T(x,\psi)/\left[p(x) \right]^{(\gamma-1)/\gamma} = T_w(\psi)/\left[p_w(\psi) \right]^{(\gamma-1)/\gamma} \tag{13}$$

Given that all streamlines are initiated through surface injection at $r = a$, Eq. (11) may be evaluated at the sidewall. This is performed while using the ideal gas expression for the density. Subsequent integration in the axial direction yields

$$\psi = \frac{a\gamma}{(\gamma-1)c_p} \int_0^\xi \left[U_w(x) p(x) / T_w(x) \right] \mathrm{d}x \tag{14}$$

As depicted in Fig. 1, ξ denotes the distance from the headwall to the point where the streamline originates at the sidewall. Since a unique value of ψ may be associated with a given ξ, one may transform the independent variables from (x,ψ) to (x,ξ). In this new coordinate system, Eqs. (12) and (13) may be written as

$$T(x,\xi) + u^2(x,\xi)/(2c_p) = T_w(\xi) \tag{15}$$

$$T(x,\xi)/\left[p(x) \right]^{(\gamma-1)/\gamma} = T_w(\xi)/\left[p(\xi) \right]^{(\gamma-1)/\gamma} \tag{16}$$

Next, the expression for the stream function given by Eq. (14) may be substituted into Eq. (10) and integrated in the radial direction. This enables us to deduce the coordinate r associated with a given axial position x and streamline emanating from ξ:

$$r^2 = 2a\int_0^\xi \left[\frac{T(x,\xi')}{p(x)u(x,\xi')}\right]\left[\frac{U_w(\xi')p(\xi')}{T_w(\xi')}\right]d\xi' \tag{17}$$

One can also replace the variables u and T using Eqs. (15) and (16) to produce an expression solely in terms of the pressure. This operation yields

$$r^2 = 2a\int_0^\xi \left[\frac{p(\xi')}{p(x)}\right]^{1/\gamma}\left[1-\left[\frac{p(x)}{p(\xi')}\right]^{(\gamma-1)/\gamma}\right]^{-1/2}\frac{U_w(\xi')}{\sqrt{2c_pT_w(\xi')}}d\xi' \tag{18}$$

At this point, we are ready to evaluate Eq. (18) knowing that $\xi = x$ at $r = a$; we get

$$a = 2\int_0^x \left[\frac{p(\xi)}{p(x)}\right]^{1/\gamma}\left[1-\left[\frac{p(x)}{p(\xi)}\right]^{(\gamma-1)/\gamma}\right]^{-1/2}\frac{U_w(\xi)}{\sqrt{2c_pT_w(\xi)}}d\xi \tag{19}$$

E. Integral Formulation with No Pressure Dependence

The dimensionless variables $P(X)$, X and Ξ may be introduced to simplify the analysis. These are defined according to

$$P(X) = \frac{p(x)}{p_0} \tag{20}$$

$$X = \sqrt{\frac{\gamma}{\gamma-1}}\frac{1}{a}\int_0^x \frac{U_w(x')}{\sqrt{2c_pT_w(x')}}dx' \tag{21}$$

$$\Xi = \sqrt{\frac{\gamma}{\gamma-1}}\frac{1}{a}\int_0^\xi \frac{U_w(x')}{\sqrt{2c_pT_w(x')}}dx' \tag{22}$$

While the normalization of P is straightforward, that of X and Ξ is based on their upper integral bounds. The dimensionless expressions are then inserted into Eqs. (18) and (19) to obtain

$$\left(\frac{r}{a}\right)^2 = 2\sqrt{\frac{\gamma-1}{\gamma}}\int_0^\Xi \left[\frac{P(\Xi')}{P(X)}\right]^{1/\gamma}\left[1-\left(\frac{P(X)}{P(\Xi')}\right)^{(\gamma-1)/\gamma}\right]^{-1/2}d\Xi' \tag{23}$$

$$\sqrt{\frac{\gamma}{\gamma-1}} = 2\int_0^X \left[\frac{P(\Xi)}{P(X)}\right]^{1/\gamma}\left[1-\left(\frac{P(X)}{P(\Xi)}\right)^{(\gamma-1)/\gamma}\right]^{-1/2}d\Xi \tag{24}$$

Equations (23) and (24) differ from the result obtained by Balakrishnan, Liñan and Williams[26] who (inadvertently) include an extra (Ξ/X) term as part of their integrand.

F. Integral Formulation with Pressure Dependence

One can also link $U_w(\xi)$ to $p(\xi)$ by assuming a dependence on the burning-rate that follows Saint-Robert's law with constant K and n,

$$m_w = \rho_w U_w = Kp^n \tag{25}$$

where m_w represents the mass flux at the wall. Then using the ideal gas law to eliminate the density, the injection velocity may be expressed as

$$U_w = \left(\frac{\gamma-1}{\gamma}\right)c_p \frac{T_w(\xi)}{p(\xi)}m_w(\xi) \tag{26}$$

After substituting the above into Eq. (19), the dimensionless forms of $P(X)$, X and Ξ are updated to obtain

$$P(X) = \frac{p(x)}{p_0} \tag{27}$$

$$X = \sqrt{\frac{\gamma-1}{\gamma}}\frac{Kp_0^{n-1}}{2a}\int_0^x \sqrt{2c_pT_w(x')}dx' \tag{28}$$

$$\Xi = \sqrt{\frac{\gamma-1}{\gamma}} \frac{Kp_0^{n-1}}{2a} \int_0^\xi \sqrt{2c_p T_w(x')} \, dx' \tag{29}$$

At length, Eqs. (18) and (19) become

$$\left(\frac{r}{a}\right)^2 = 2\sqrt{\frac{\gamma-1}{\gamma}} \int_0^\Xi \left[P(\Xi')\right]^{n-1} \left[\frac{P(\Xi')}{P(X)}\right]^{1/\gamma} \left[1 - \left(\frac{P(X)}{P(\Xi')}\right)^{(\gamma-1)/\gamma}\right]^{-1/2} d\Xi' \tag{30}$$

$$\sqrt{\frac{\gamma}{\gamma-1}} = 2\int_0^X \left[P(\Xi)\right]^{n-1} \left[\frac{P(\Xi)}{P(X)}\right]^{1/\gamma} \left[1 - \left(\frac{P(X)}{P(\Xi)}\right)^{(\gamma-1)/\gamma}\right]^{-1/2} d\Xi \tag{31}$$

The procedure for solving this problem consists of integrating Eq. (31) to the extent of determining the pressure as a function of x. Equation (30) can then be evaluated to deduce the radial coordinate in terms of x and ξ. With the pressure distribution at hand, the temperature can be obtained using the isentropic relation of Eq. (16). The velocity may then be extracted from the total temperature relation given by Eq. (15).

For the calculation of the Mach number, one can employ the compressible flow relation $M = u / \sqrt{(\gamma-1)c_p T}$. In fact, the substitution of Eq. (15) into the Mach number relation gives

$$M = \sqrt{\left(\frac{2}{\gamma-1}\right)\left[\frac{T_w(\xi)}{T(x,\xi)} - 1\right]} = \sqrt{\left(\frac{2}{\gamma-1}\right)\left[\left(\frac{P(\Xi)}{P(X)}\right)^{(\gamma-1)/\gamma} - 1\right]} \tag{32}$$

where the right-hand-side expression may be obtained using the isentropic identity given by Eq. (16).

G. Numerical Procedure

For the numerical integration of Eq. (31), an inverse procedure may be pursued. This is accomplished by switching to P as the independent variable and calculating X in increments of ΔP. The scheme begins at the headwall boundary, where $X = 0$ at $P = 1$. Choking conditions occur when $dP/dX \to \infty$ at a pressure denoted by P_c. Transforming the independent variable in Eq. (31) results in

$$2\sqrt{\frac{\gamma-1}{\gamma}} \int_P^1 (P')^{n-1} \left(\frac{P'}{P}\right)^{1/\gamma} \left[1 - \left(\frac{P}{P'}\right)^{(\gamma-1)/\gamma}\right]^{-1/2} \left[-\frac{dX(P')}{dP'}\right] dP' = \int_P^1 f(P') dP' = 1 \tag{33}$$

In order to overcome the singularities at the boundaries, we split the integral into three parts:

$$\int_P^1 f(P') dP' = \underbrace{\int_{P_i}^{P_{i-1}} f(P') dP'}_{1} + \underbrace{\int_{P_{i-1}}^{1-\Delta P} f(P') dP'}_{2} + \underbrace{\int_{1-\Delta P}^1 f(P') dP'}_{3} = 1 \tag{34}$$

In the region near $P = P_i$, we approximate the first integrand and retrieve an expression that can be readily evaluated for an arbitrary pressure exponent n,

$$\int_{P_i}^{P_{i-1}} f(P') dP' \approx 2\int_{P_i}^{P_{i-1}} (P')^{n-1} \left(\frac{P'-P_i}{P'}\right)^{-1/2} \left(-\frac{dX}{dP}\right)_i dP' \tag{35}$$

The second integral may be computed, let us say, using the trapezoidal rule. This involves finite step discretization,

$$\int_{P_{i-1}}^{1-\Delta P} f(P') dP' \approx \Delta P \left(\frac{f_1 + f_{i-1}}{2} + \sum_{k=2}^{i-2} f_k\right) \tag{36}$$

where

$$f_k = 2\sqrt{\frac{\gamma-1}{\gamma}} \left[P_k\right]^{n-1} \left[\frac{P_k}{P_i}\right]^{1/\gamma} \left[1 - \left(\frac{P_i}{P_k}\right)^{(\gamma-1)/\gamma}\right]^{-1/2} \left(-\frac{dX}{dP}\right)_k \tag{37}$$

In the third integral, where X is small, $P(X)$ may be expanded using a polynomial of the form

$$P(X) = 1 - \alpha X^2 + \dots \tag{38}$$

By inserting Eq. (38) into the integral and assuming $\alpha \Xi^2 \ll 1$, we are left with

$$\int_{1-\Delta P}^1 f(P') dP' \approx 2\sqrt{\frac{\gamma-1}{\gamma}} (P_i)^{-1/\gamma} \left[1 - (P_i)^{(\gamma-1)/\gamma}\right]^{-1/2} \sqrt{\frac{\Delta P}{\alpha}} \tag{39}$$
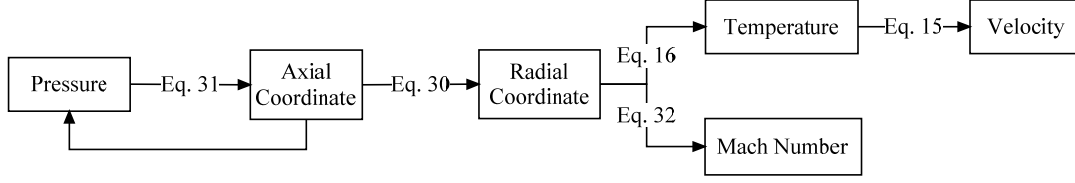
Figure 2. Flowchart depicting the main steps of the numerical procedure needed to extract the velocity from the integral formulation of the pressure.

To evaluate Eq. (39), α must be known beforehand. This is achieved by substituting Eq. (38) into Eq. (31) and returning

$$\frac{2}{\sqrt{\alpha}}\int_0^X \frac{1}{\sqrt{X^2-\Xi^2}}\,d\Xi = 1 \tag{40}$$

This enables us to deduce that $\alpha = \pi^2$.

Equation (34) is now linear in X_i. Starting with $X=0$ at $P=1$, one may solve for X_i at every step until choking conditions are reached. Choking occurs at a point where P approaches its limiting value P_c at an infinitely steep slope and where the average Mach number reaches unity. With the pressure distribution fully determined, it may be employed in Eq. (30) and integrated numerically. This returns r which is needed for the complete description of the streamlines. Equations (15) and (16) may then be utilized to extract the temperature and velocity. This process is illustrated in the flowchart diagram posted as Fig. 2.

III. Results and Discussion

After solving Eq. (33) in decrements of ΔP, the pressure is reproduced as a function of the axial distance. The resulting solutions for P and T are showcased in Fig. 3 for $n=0$ and $n=1$. Also shown on the graphs are the analytical predictions based on the one-dimensional theory of Gany and Aharon[19] and the two-dimensional analysis of Majdalani.[28]

Based on Fig. 3, a qualitative agreement may be seen to be established between the present, semi-analytical formulation, and Majdalani's closed form solution.[28] The same may be said concerning the one-dimensional solution of Gany and Aharon[19] despite its entirely dissimilar form. The small differences separating these estimates may be attributed to their underlying assumptions. On the one hand, the instantaneous burning rate of the one-dimensional solution[19] is taken to be uniform along the grain, thus leading to a constant mass flux at the simulated propellant surface. A corresponding relation may be reproduced in the present solution by setting $n=0$, as reflected in the improved agreement with one-dimensional theory that may be inferred from Figs. 3a-b. Note that the one-dimensional model yields[19]

$$M_{1D} = \sqrt{\frac{1-\sqrt{1-\chi^2}}{1+\gamma\sqrt{1-\chi^2}}};\chi \equiv \frac{x}{L_s},\quad P_{1D} = (1+\gamma)^{-1}\left(1+\gamma\sqrt{1-\chi^2}\right),\quad T_{1D} = (1+\gamma)^{1/\gamma-1}\left(1+\gamma\sqrt{1-\chi^2}\right)^{1-1/\gamma} \tag{41}$$

On the other hand, the uniform sidewall injection velocity of the two-dimensional axisymmetric solution of Majdalani[28] corresponds to the $n=1$ case presented here. This may also explain the improved agreement with two-dimensional theory in Figs. 3c-d. In the interest of clarity, the two-dimensional solution obtained by Majdalani[28] is reproduced below:

$$\psi = M_w\psi_0\left(1-\tfrac{1}{4}\Gamma^2\left[1+\tfrac{1}{3}\cos(\pi r^2)\right]\chi^2+\tfrac{1}{2}M_w^2\right);\psi_0 = x\sin(\tfrac{1}{2}\pi r^2) \text{ (stream funtion)} \tag{42}$$

$$M_c = \Gamma\chi\frac{2+\tfrac{1}{3}\Gamma^2\chi^2-M_w^2}{\sqrt{4-2(\gamma-1)\Gamma^2\chi^2}};\text{ (centerline Mach number)} \tag{43}$$

$$p_c = 1-\tfrac{1}{2}\gamma\Gamma^2\chi^2(1-M_w^2)-\tfrac{1}{24}\gamma\Gamma^4\chi^4 \text{ (centerline pressure)} \tag{44}$$

$$T_c = 1-\tfrac{1}{2}(\gamma-1)\Gamma^2\chi^2(1-M_w^2)-\tfrac{1}{6}(\gamma-1)\Gamma^4\chi^4 \text{ (centerline temperature)} \tag{45}$$

where the sonic length, also known as the critical distance, is related to the Γ function through

$$\Gamma \equiv \pi M_w L_s = \sqrt{\lambda-2\gamma-2+2(2\gamma^2+\gamma-1)/\lambda}$$
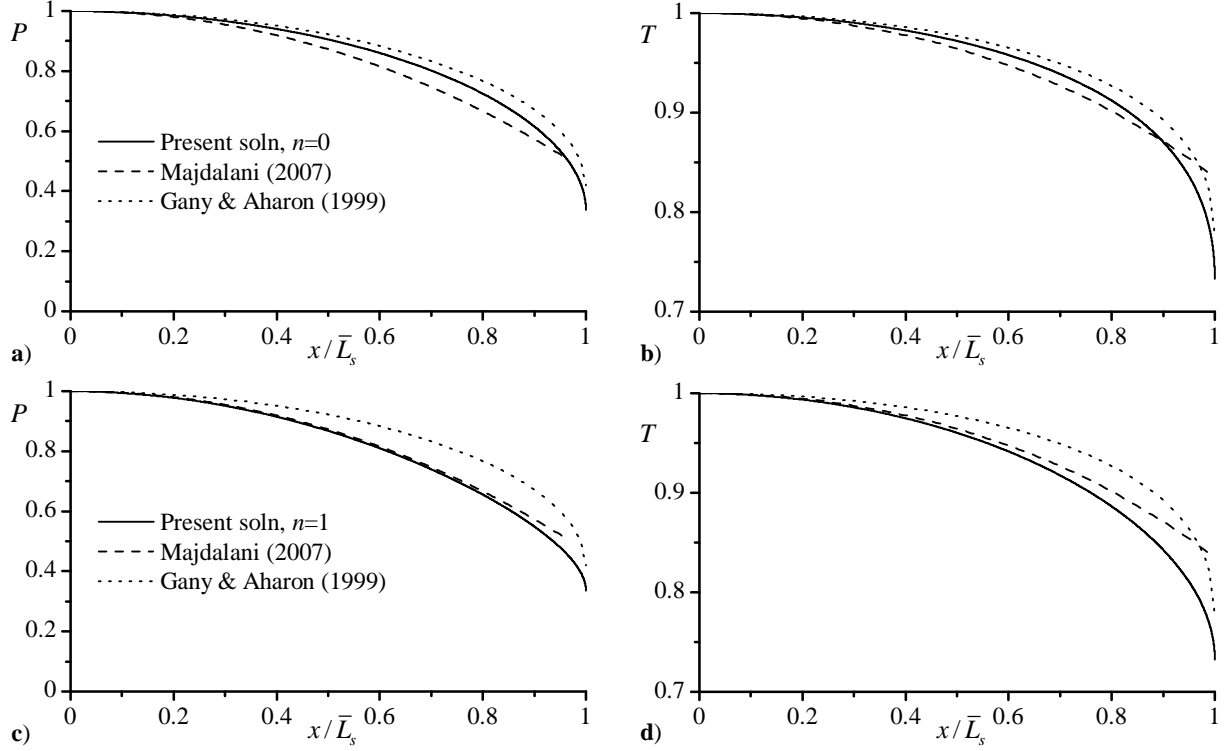
Figure 3. Comparison between the present semi-analytical formulation and both 1D and 2D solutions by Gany & Aharon (1999) and Majdalani (2007). Results are shown for $\gamma = 1.4$ and $M_w = 0.05$.

$$\cong 0.884622 - 0.177299(\gamma-1) + 0.0539119(\gamma-1)^2 - 0.0180615(\gamma-1)^3 \tag{46}$$

and

$$\lambda = \left(28 + 12\gamma - 6\gamma^2 - 8\gamma^3 + 6\sqrt{22 + 18\gamma - 6\gamma^2 - 14\gamma^3 - 3\gamma^4}\right)^{1/3} \tag{47}$$

In Figs. 3a-b, the reason for the slight discrepancy at $n=0$ may be attributed to the dismissal of radial pressure variations in the pseudo-two-dimensional formulation. As for the $n=1$ case, the present model appears to be in excellent agreement with Majdalani's solution everywhere except in the vicinity of the choke point. Specifically, the tailing ends of the numerical curves in Figs. 3c-d suddenly undergo an abrupt steepening process as the choke point is approached, thus leading to a slight discrepancy with Majdalani's two-dimensional formulation.[28] Two possible explanations may be offered in this respect. The first attributes the attendant divergence to the dismissal of radial pressure variations in the semi-analytical formulation, and to the polynomial approximation affecting pressure integration in Eq. (39). These approximations are likely to deteriorate near the choke point. The second source of disparity may be connected to the accuracy of Majdalani's Rayleigh-Janzen expansion in the vicinity of $x = \bar{L}_s$. However, according to Tollmien[30] and Kaplan,[31] it is formally proven that the Rayleigh-Janzen paradigm continues to be robust past sonic conditions. The first explanation is hence more plausible. On a separate subject, we remind the reader that the four parts of Fig. 3 are obtained with an injection wall Mach number of 0.05. Nonetheless, these plots remain rather universal and therefore characteristic of the solution at other wall Mach numbers as well. This may be attributed to the results being displayed as function of the geometric similarity coordinate, $x / \bar{L}_s$. As one may surmise from Eqs. (42)-(45), the similarity with respect to $x / \bar{L}_s$ leads to a virtual independence of M_w.

Concerning the calculation of the critical length, our computation of L_s leads to a sonic distance that matches quite closely the value predicted by Eq. (46). On this note, it should be borne in mind that, according to Majdalani,[28] the critical length denotes in the classic sense the distance from the headwall to the point at which the centerline velocity first reaches the speed of sound. At that station, the area-averaged Mach number would not have reached unity yet. However, in order to reconcile with one-dimensional predictions in which values are essentially
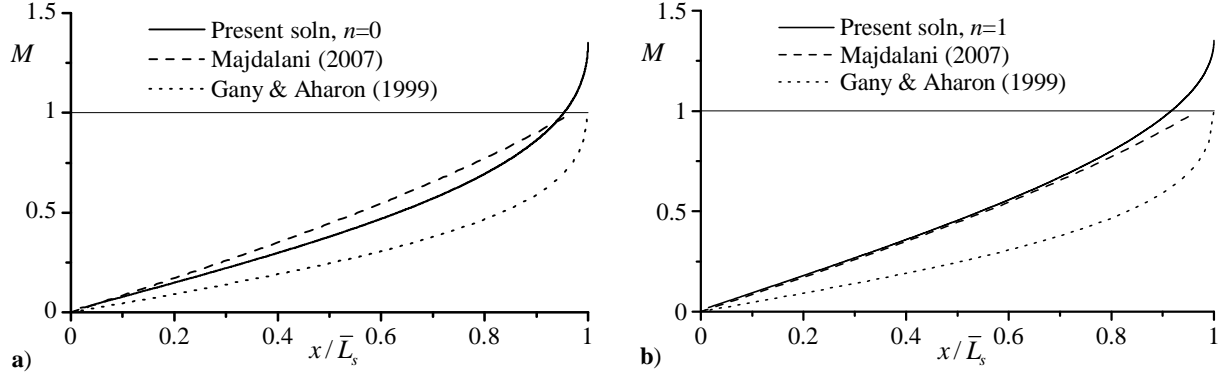
Figure 4. Evolution of centerline Mach numbers along with available 1D and 2D solutions. Here $\gamma = 1.4$ and $M_w = 0.05$.
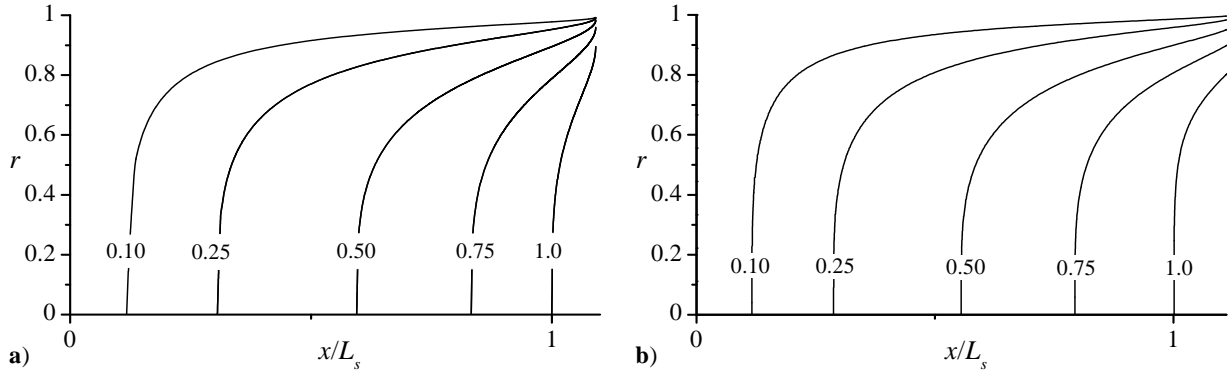
Figure 5. Local Mach number contours according to a) numerical integration and b) analytical solution by Majdalani.[28] Here $\gamma = 1.4$ and $M_w = 0.01$.

area-averaged at a given axial station, a new definition is warranted, namely, of an area-averaged critical length, $\bar{L}_s$. In this vein, a cross-section will be fully choked when the average Mach number reaches unity. This condition always occurs at $\bar{L}_s > L_s$, with a typical $\bar{L}_s \approx 1.2 L_s$.

Using $\bar{L}_s$ in lieu of L_s, a comparison of the centerline Mach numbers is provided in Figs. 4a,b for $n = 0$ and $n = 1$, respectively. In both parts of this figure, the 2D analytical model is seen to outperform the 1D solution although better agreement with the integral representation appears in Fig. 4b. This behavior may be naturally expected because the 2D model is derived under the $n = 1$ assumption. Another point of disparity may be associated with the centerline Mach numbers exceeding unity at $x = \bar{L}_s$. Conversely, the 1D Mach number, in which area-averaging is intrinsic, is seen to reach sonic conditions at $x = \bar{L}_s$. Although not shown, the analytical area-averaged Mach number and, in principle, the numerically area-averaged solution of the present formulation will exhibit steeper curvatures that closely follow the dotted, 1D line.[28]

It may be instructive to add that, based on Eq. (32), the Mach number may be calculated over the entire chamber. However, owing to the variables being expressed in terms of the axial location and the stream function "tip" ξ, a transformation is required to convert ξ back to the radial coordinate by way of Eq. (30). The results lead to a non-uniform mesh that requires careful treatment and "reverse engineering." After some effort, the contour plots of the numerically extracted local Mach numbers are displayed in Fig 5a, where the shape of the $M = 1$ curve is clearly delineated. The two-dimensional analytical predictions of the iso-Mach number lines are presented side-by-side in Fig. 5b. Despite the dissimilarity in the contour curvature near choking (upper rightmost corner), the two models appear to be in fairly good agreement. Note that the traditional choking point is rather a curved line and, in reality, a surface due to axisymmetry, that can be captured either numerically, or analytically for $M = 1$. Note that Figs. 4 and 5 are essentially universal and, being plotted versus $\chi = x / L_s$, will not change if a different wall Mach number is used to reproduce them. This again is due to the geometric self-similarity with respect to χ that may be inferred from Eqs. (42)-(45).

Having completed our description of the Mach number variation, characteristic streamlines are displayed in Fig. 6 based on the numerical integration of Eq. (30). This is carried out by first specifying a value of ξ, and then integrating at discrete locations of x until the centerline Mach number has reached unity. This marks the critical distance to the sonic point and enables us to calculate L_s for each of the test cases at hand. The procedure also enables us to collect the family of coordinates at a fixed value of ξ, thus leading to an assortment of points that constitute a streamline. By comparing the results in Fig. 6 at two wall Mach numbers of a) 0.01 and b) 0.005, it is clear that compressibility becomes more pronounced when the mean flow velocity is increased (here $\gamma = 1.4$). This is reflected in the faster flow turning that occurs at higher injection Mach numbers, specifically faster in Fig. 6a where $L_s \cong 24.44$, than in Fig. 6b where $L_s \cong 48.87$. However, by replotting these two cases versus x/L_s in Figs. 6c,d, the ensuing graphs become identical! This is caused by the strong similarity with respect to χ.
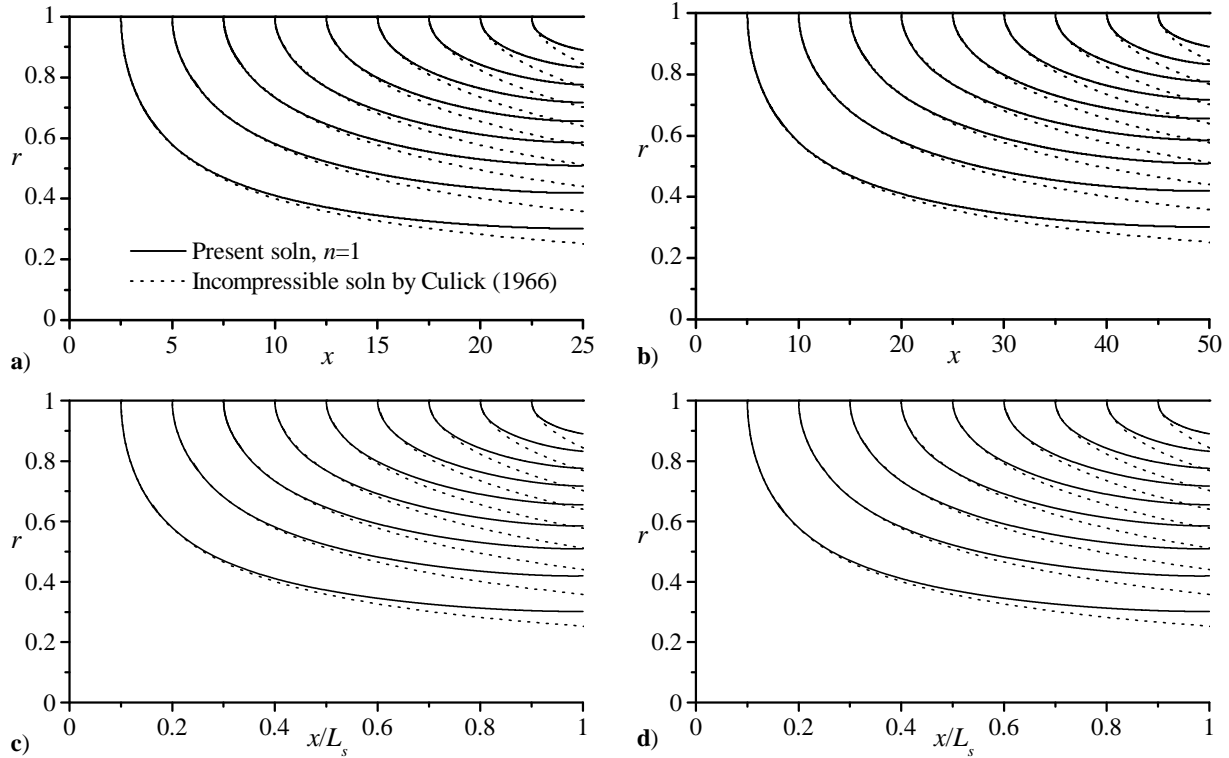
Figure 6. Numerical streamlines for a,c) $M_w = 0.01$ and b,d) $M_w = 0.005$ compared to the incompressible solution by Culick (1966). In c-d) the axial coordinate is rescaled by the critical length, thus leading to self-similarity. Here $\gamma = 1.4$.
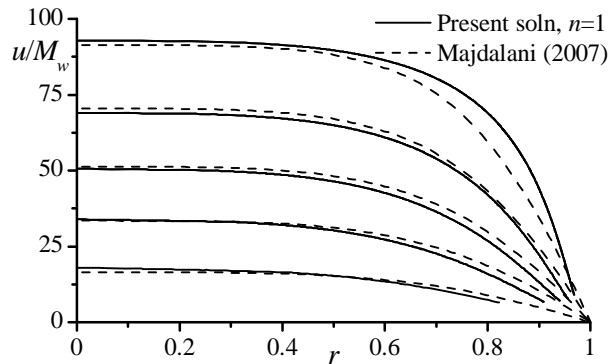
Figure 7. Spatial evolution of the axial velocity for $M_w = 0.01$ at $x/L_s \approx 0.2, 0.4, 0.6, 0.8$, and 1. Results are compared to the 2D axisymmetric solution by Majdalani.[28] Here $\gamma = 1.4$.

As sketched in Fig. 2, the last procedural step consists of extracting the axial velocity from Eq. (15). Results are shown in Fig. 7 at evenly spaced intervals of $x/L_s \approx 0.2, 0.4, \ldots, 1$. Also featured on the graph is Majdalani's 2D analytical solution.[28] As expected, these profiles bear a striking resemblance to the numerical results and to both laboratory and computational experiments obtained by Traineau, Hervat and Kuentzmann,[13] Balakrishnan, Liñan and Williams,[27] Apte and Yang,[17-18] and others. By comparison to Taylor-Culick's incompressible mean flow solution,[1] we note that the streamwise velocity develops into a much fuller, top-hat profile as choking is approached. The evolution into a blunter, turbulent-like, or pseudo-one-dimensional plug flow is conformant to both theory and experiment. It faithfully captures the increased gradients at the sidewall and these can have important implications in mean-flow related analyses.

IV. Conclusions

The integral formulation of the axisymmetric porous cylinder that was initiated by Traineau, Hervat and Kuentzmann[13] is reconstructed and compared to one- and two-dimensional analytical approximations obtained under isentropic flow conditions. Unsurprisingly, the level of agreement with the integral representation is found to be commensurate with the sidewall boundary conditions associated with each of these models. Being derived for a uniform mass flux at the sidewall, the one-dimensional model seems to provide closer predictions to the inverted integral solution with a pressure exponent of $n = 0$. Such a condition suppresses the velocity dependence on the pressure and ensures a constant mass flux at the sidewall. Conversely, the $n = 1$ case leads to a constant wall-normal velocity that coincides with one of the boundary conditions used in deriving the two-dimensional analytical model.[28] Consequently, numerical predictions for this case fall in closer agreement with the two-dimensional solution. In all cases, the main discrepancies occur near the sonic point and may be attributed to the various forms of approximations and linearizations befalling the integral approach. Furthermore, when comparing the level of difficulty needed to reproduce these solutions, the closed-form analytical approximations seem to substantially outperform the semi-analytical treatment. The latter requires piecewise numerical integrations, sequential inversions, and backward transformations to retrieve the original variables of interest. As if these multiple operations are not enough, the problem is further exacerbated by the variable extraction process occurring over a highly non-uniform mesh. This can render simple steps extraordinarily challenging especially when attempting to extrapolate other related variables and derivatives that are needed over a uniform grid. Such effort can be quite laborious when compared to the ease with which the fully analytical models are implemented and resolved. Nonetheless, the numerical formulation helps to confirm several useful characteristics associated with the two-dimensional theory introduced previously by Majdalani.[28] Among them is the strong, albeit non-exact, self-similarity with respect to the critical length. This can be seen by rescaling the axial coordinate with respect to $x = L_s$; numerically obtained streamline, pressure, and temperature plots taken at two different Mach numbers become visually identical. The observed behavior confirms two-dimensional theory which, in turn, projects deviations from self-similarity to be of the order of the wall Mach number squared, a practically small quantity that leads to relative differences of less than 1%.

Acknowledgments

References

[1]Culick, F. E. C., "Rotational Axisymmetric Mean Flow and Damping of Acoustic Waves in a Solid Propellant Rocket," *AIAA Journal,* Vol. 4, No. 8, 1966, pp. 1462-1464.

[2]Dunlap, R., Blackner, A. M., Waugh, R. C., Brown, R. S., and Willoughby, P. G., "Internal Flow Field Studies in a Simulated Cylindrical Port Rocket Chamber," *Journal of Propulsion and Power,* Vol. 6, No. 6, 1990, pp. 690-704.

[3]Saad, T., and Majdalani, J., "Rotational Flowfields in Porous Channels with Arbitrary Headwall Injection," *Journal of Propulsion and Power,* Vol. 25, No. 4, 2009, pp. 921-929.

[4]Majdalani, J., and Saad, T., "The Taylor-Culick Profile with Arbitrary Headwall Injection," *Physics of Fluids,* Vol. 19, No. 9, 2007, pp. 093601-10.

[5]Zhou, C., and Majdalani, J., "Improved Mean Flow Solution for Slab Rocket Motors with Regressing Walls," *Journal of Propulsion and Power,* Vol. 18, No. 3, 2002, pp. 703-711.

[6]Majdalani, J., Vyas, A. B., and Flandro, G. A., "Higher Mean-Flow Approximation for a Solid Rocket Motor with Radially Regressing Walls," *AIAA Journal,* Vol. 40, No. 9, 2002, pp. 1780-1788.

[7]Sams, O. C., Majdalani, J., and Saad, T., "Mean Flow Approximations for Solid Rocket Motors with Tapered Walls," *Journal of Propulsion and Power,* Vol. 23, No. 2, 2007, pp. 445-456.

[8]Saad, T., Sams, O. C., and Majdalani, J., "Rotational Flow in Tapered Slab Rocket Motors," *Physics of Fluids,* Vol. 18, No. 1, 2006, pp. 103601-13.

[9]Kurdyumov, V. N., "Steady Flows in the Slender, Noncircular, Combustion Chambers of Solid Propellants Rockets," *AIAA Journal,* Vol. 44, No. 12, 2006, pp. 2979-2986.

[10]Majdalani, J., and Saad, T., "Energy Steepened States of the Taylor-Culick Profile," AIAA Paper 2007-5797, July 2007.

[11]Saad, T., and Majdalani, J., "Energy Based Mean Flow Solutions for Slab Hybrid Rocket Chambers," AIAA Paper 2008-5021, July 2008.

[12]Dunlap, R., Willoughby, P. G., and Hermsen, R. W., "Flowfield in the Combustion Chamber of a Solid Propellant Rocket Motor," *AIAA Journal,* Vol. 12, No. 10, 1974, pp. 1440-1445.

[13]Traineau, J. C., Hervat, P., and Kuentzmann, P., "Cold-Flow Simulation of a Two-Dimensional Nozzleless Solid-Rocket Motor," AIAA Paper 86-1447, July 1986.

[14]Beddini, R. A., "Injection-Induced Flows in Porous-Walled Ducts," *AIAA Journal,* Vol. 24, No. 11, 1986, pp. 1766-1773.

[15]Baum, J. D., Levine, J. N., and Lovine, R. L., "Pulsed Instabilities in Rocket Motors: A Comparison between Predictions and Experiments," *Journal of Propulsion and Power,* Vol. 4, No. 4, 1988, pp. 308-316.

[16]Liou, T.-M., and Lien, W.-Y., "Numerical Simulations of Injection-Driven Flows in a Two-Dimensional Nozzleless Solid-Rocket Motor," *Journal of Propulsion and Power,* Vol. 11, No. 4, 1995, pp. 600-606.

[17]Apte, S., and Yang, V., "Effect of Acoustic Oscillation on Flow Development in a Simulated Nozzleless Rocket Motor," *Solid Propellant Chemistry, Combustion, and Motor Interior Ballistics*, Vol. 185, edited by V. Yang, T. B. Brill, and W.-Z. Ren, AIAA Progress in Astronautics and Aeronautics, Washington, DC, 2000, pp. 791-822.

[18]Apte, S., and Yang, V., "Unsteady Flow Evolution in a Porous Chamber with Surface Mass Injection. Part I: Free Oscillation," *AIAA Journal,* Vol. 39, No. 8, 2001, pp. 1577-1586.

[19]Gany, A., and Aharon, I., "Internal Ballistics Considerations of Nozzleless Rocket Motors," *Journal of Propulsion and Power,* Vol. 15, No. 6, 1999, pp. 866-873.

[20]King, M. K., "Consideration of Two-Dimensional Flow Effects on Nozzleless Rocket Performance," *Journal of Propulsion and Power,* Vol. 3, No. 3, 1987, pp. 194-195.

[21]Venugopal, P., Najjar, F. M., and Moser, R. D., "Numerical Simulations of Model Solid Rocket Motor Flows," AIAA Paper 2001-3950, July 2001.

[22]Wasistho, B., Balachandar, S., and Moser, R. D., "Compressible Wall-Injection Flows in Laminar, Transitional, and Turbulent Regimes: Numerical Prediction," *Journal of Spacecraft and Rockets,* Vol. 41, No. 6, 2004, pp. 915-924.

[23]Najjar, F. M., Haselbacher, A., Ferry, J. P., Wasistho, B., Balachandar, S., and Moser, R., "Large-Scale Multiphase Large-Eddy Simulation of Flows in Solid-Rocket Motors," AIAA Paper 2003-3700, June 2003.

[24]Wasistho, B., Haselbacher, A., Najjar, F. M., Tafti, D., Balachandar, S., and Moser, R. D., "Direct and Large Eddy Simulations of Compressible Wall-Injection Flows in Laminar, Transitional, and Turbulent Regimes," AIAA Paper 2002-4344, July 2002.

[25]Shapiro, A. H., *The Dynamics and Thermodynamics of Compressible Fluid Flow*, Vol. 1, The Ronald Press Company, 1953.

[26]Balakrishnan, G., Liñan, A., and Williams, F. A., "Compressible Effects in Thin Channels with Injection," *AIAA Journal,* Vol. 29, No. 12, 1991, pp. 2149-2154.

[27]Balakrishnan, G., Liñan, A., and Williams, F. A., "Rotational Inviscid Flow in Laterally Burning Solid Propellant Rocket Motors," *Journal of Propulsion and Power,* Vol. 8, No. 6, 1992, pp. 1167-1176.

[28]Majdalani, J., "On Steady Rotational High Speed Flows: The Compressible Taylor-Culick Profile," *Proceedings of the Royal Society, London, Series A,* Vol. 463, No. 2077, 2007, pp. 131-162.

[29]Maicke, B. A., and Majdalani, J., "On the Rotational Compressible Taylor Flow in Injection-Driven Porous Chambers," *Journal of Fluid Mechanics,* Vol. 603, No. 1, 2008, pp. 391-411.

[30]Tollmien, W., "Grenzlinien Adiabatischer Potentialströmungen.," *Zeitschrift für angewandte Mathematik und Mechanik,* Vol. 21, No. 3, 1941, pp. 140-152.

[31]Kaplan, C., "Effect of Compressibility at High Subsonic Velocities on the Lifting Force Acting on an Elliptic Cylinder," Langley Memorial Aeronautical Laboratory, National Advisory Committee for Aeronautics, NACA Rept. 834, Langley Field, VA, May 16 1946.